Journal of Magnetic Resonance 193 (2008) 259–266

Contents lists available at ScienceDirect

Journal of Magnetic Resonance

journal homepage: www.elsevier.com/locate/jmr

Magnetic resonance imaging of water content across the Nafion membrane in an operational PEM fuel cell

Ziheng Zhang [a], Jonathan Martin [b], Jinfeng Wu [b], Haijiang Wang [b], Keith Promislow [c], Bruce J. Balcom [a,*]

[a] MRI Centre, Department of Physics, University of New Brunswick, Fredericton, New Brunswick, Canada E3B 5A3
[b] Institute for Fuel Cell Innovation (IFCI), National Research Council of Canada, 4250 Wesbrook Mall, Vancouver, BC, Canada V6T 1W5
[c] Department of Mathematics, Michigan State University, East Lansing, MI 48824, USA

ARTICLE INFO

Article history:
Received 11 February 2008
Revised 19 April 2008
Available online 16 May 2008

Keywords:
Water transport
Nafion
Fuel cell
SE SPI
MRI
Imaging
Magnetic resonance
Water management

ABSTRACT

Water management is critical to optimize the operation of polymer electrolyte membrane fuel cells. At present, numerical models are employed to guide water management in such fuel cells. Accurate measurements of water content variation in polymer electrolyte membrane fuel cells are required to validate these models and to optimize fuel cell behavior.

We report a direct water content measurement across the Nafion membrane in an operational polymer electrolyte membrane fuel cell, employing double half *k*-space spin echo single point imaging techniques. The MRI measurements with T_2 mapping were undertaken with a parallel plate resonator to avoid the effects of RF screening. The parallel plate resonator employs the electrodes inherent to the fuel cell to create a resonant circuit at RF frequencies for MR excitation and detection, while still operating as a conventional fuel cell at DC.

Three stages of fuel cell operation were investigated: activation, operation and dehydration. Each profile was acquired in 6 min, with 6 μm nominal resolution and a SNR of better than 15.

1. Introduction

Polymer electrolyte membrane (PEM) fuel cells have the potential to become major alternative power sources for automotive and stationary power applications because of their high efficiency and benign emissions [1–3].

The efficiency of PEM fuel cells, determined by the proton mobility and concentration, varies with the water content of the membrane. Excess water is produced at the cathode during fuel cell operation. This water may accumulate and prevent sufficient reactant gas transport. Too little water retained at the anode reduces the local membrane ionic conductivity. Management of the water content across the membrane to optimize the PEM fuel cell performance [4,5] relies on understanding the proton conductivity, water diffusion coefficient, and electro-osmotic drag coefficient—all as functions of water content in the membrane [6]. There is still a lack of direct measurements to validate phenomenological models, which are relied on to guide fuel cell operation at present [7,8].

Two literature studies have directly measured the water content across the PEM in operational fuel cells. Bellow et al., used neutron radiography [9], and Teranishi et al. used traditional ^{1}H NMR frequency encoded imaging [10,11]. However, due to the inherent limitations of these techniques, neither produces high quality water content profiles, with adequate spatial resolution. Many other studies employing bulk NMR or conventional 2D MRI to characterize the Nafion in an operating fuel cell have been reported [12–18]. None monitored the water content distribution across Nafion in an operating fuel cell with high resolution. We, and others, believe that MRI will be able to make a significant contribution to PEM fuel cell research, but dedicated techniques must be developed.

Double half *k*-space (DHK) spin echo (SE) single point imaging (SPI) [19], specially designed for high resolution thin film depth imaging, is a pure phase encoding technique, which yields images free from distortions due to B_0 inhomogeneity, susceptibility variations, and chemical shift [20,21]. In previous work employing this technique, the water content across Nafion 1110 within a mock fuel cell under well controlled boundary conditions was explored [22]. Water inside the Nafion membrane has high mobility, and redistributes rapidly. T_2 mapping with the DHK SE SPI method permitted ready discrimination of T_2 contrast and water content variation in the images. T_2 is well known to vary with water content in Nafion.

The surface coil is a natural choice for thin film depth imaging [23], due to its high local B_1 strength and sensitivity. In normal use, it would be positioned above or below the film with B_1 perpendicular to the sample plane. To excite a realistic fuel cell

* Corresponding author. Fax: +1 506 453 4581.
E-mail address: bjb@unb.ca (B.J. Balcom).

1090-7807/$ - see front matter © 2008 Elsevier Inc. All rights reserved.
doi:10.1016/j.jmr.2008.05.005

system, however, the surface coil is not a good choice, as the conductive layers of the fuel cell (gas diffusion layer and current collector) will severely attenuate B_1 due to RF screening.

We have developed a parallel plate resonator as an alternative to the surface coil for high resolution thin film depth imaging. This novel probe design inherently avoids the skin depth problem, because it generates a B_1 field parallel to the sample plane rather than normal to it. The parallel plate resonator was designed to permit fluid transport across the film of interest during the measurement. A related probe design, contemporary with our work, has been introduced for biomedical histology [24].

In this study, a homemade fuel cell was incorporated into the RF circuit of a parallel plate resonator. The electrodes of the fuel cell are the resonating plates of the probe.

True water content profiles across a Nafion membrane in the homemade fuel cell are presented in this paper. Image profiles from the first echo, in addition to T_2 maps and true water content maps, are produced. Three stages of fuel cell operation, activation, operation, and cathode drying, representative of the whole cycle of fuel cell operation, have been studied.

2. Theory

2.1. T_2 mapping with multi-echo DHK SE SPI

Centric-scan spin echo (SE) single point imaging (SPI) has been discussed in the literature [19,22]. The multi-echo DHK SE SPI measurement generates a rapid series of T_2 weighted profiles. By fitting the profile series at each pixel to the signal equation [19],

$$S(y) = \rho_0(y) \cdot \exp\left(-\frac{n\mathrm{TE}}{T_2(y)}\right), \tag{1}$$

it is possible to spatially resolve both T_2 and the local proton density, corresponding to the water content. $\rho_0(y)$ is the local proton density, while TE is the echo time and n is the echo number.

2.2. PEM fuel cell

A basic PEM fuel cell, as shown in Fig. 1, consists of two current collectors separated by a membrane electrode assembly (MEA). The MEA typically includes two catalyst sprayed gas diffusion layers with a sheet of PEM sandwiched in the middle or two gas diffusion layers sandwiching a sheet of catalyst coated PEM.

As illustrated in Fig. 1, hydrogen gas enters the cell on the left side and oxygen enters on the right. Once the hydrogen gas diffuses across the gas diffusion layer (GDL), it encounters the catalyst layer, where hydrogen molecules oxidize and split into H^+ and electrons. The protons move through the PEM, a polymer functionalized to promote proton transfer, in association with water molecules. Liquid water moves under the action of two primary transport mechanisms: electro-osmotic drag and diffusion along concentration gradients. The electrons released at the anode travel through the external load to the cathode, where the oxygen reduction reaction consumes the electrons. At the cathode, protons and electrons react with the oxygen in the presence of another catalyst layer [3]. Water is the by-product, and heat is released.

In an operating fuel cell, non-uniform water distribution across the membrane is anticipated with a dry anode side and a much wetter cathode side. No detailed models have been developed to interpret and understand this water variation. In recent work, Weber et al. [25,26], suggested that pore-expansion based upon liquid pressure connects nanopores within the ionomer with simultaneous diffusion and permeation mass transport. This model has a degenerate transport mechanism which predicts sharp hydration fronts traversing the membrane. Clearly better experimental data will aid in the development and validation of a high quality model.

2.3. RF circuit

An operating fuel cell is a complicated electrical device, with its own resistance, capacitance and electric potential [1]. The equivalent RF circuit incorporating the operating fuel cell is illustrated in Fig. 2. The capacitance of the cell itself can be expressed as, $C_{\mathrm{in}} = \varepsilon\frac{A}{d}$, where ε is the electrical permittivity, A is the surface area and d is the separation of the plates. The resistor R_{r} models the ohmic losses, which are the effect of the electrical resistance of the electrodes and the resistance to the flow of ions in the electrolyte. R_{r} is employed to represent the ohmic voltage drop. The activation voltage drop is represented through the parallel connection of the internal capacitance, C_{in}, with a resistor, R_{a}, representing the activation and concentration losses. E models the Nernst voltage of the cell.

Theoretical prediction of the capacitance required for tuning and matching the RF probe is possible, but beyond the scope of this paper [27]. In this study, the probe was tuned and matched experimentally.

3. Results and discussion

3.1. RF probe and fuel cell

The resonant circuit, as shown in Fig. 3, consists of the main body of the fuel cell which was integrated into the RF circuit, and the electrical elements for the probe tuning and matching. The electrodes of the fuel cell were made from gold plated PC board, with slots etched on the surface as flow channels. Grooves cut into the substrate distributed the reactant gases homogeneously to the gas channels. The outlet of the reactant gases, H_2 and air, are marked in the figure. The inlet connections are on the left side of the figure. The membrane electrode assembly (MEA), composed of a piece of Nafion 1110 and two catalyst sprayed gas diffusion layers (GDL), was sandwiched by the electrodes with two home-made Teflon O-rings (only the top one is shown in the diagram). The O-rings ensure a well sealed system. Copper bolts and nuts were used to tighten the system and achieve a desired confining pressure. An outer electrical load was connected to complete the DC circuit. Capacitors, C_{c}, C_{f}, C_{b} and C_{m} were soldered to the electrodes, as illustrated in Fig. 3, to complete the RF circuit and allow probe tuning and matching.

3.2. I–V polarization curve measurement

Before integration into the RF circuit, the assembled fuel cell was examined on a load station. The cell voltage and power output as functions of cell current were measured, Fig. 4, under similar operating conditions, i.e. temperature and flow rate of the reactant gases, to those in the magnet. The polarization curve presents the three typical regions of an operational PEM fuel cell, the activation overpotential region, the ohmic region and the mass transport loss region, which are normally used to evaluate the cell's performance [3].

The steep slope of the curve in the middle part indicates high transition impedance, which is mainly from the Nafion 1110, 250 μm thickness, and partially from degradation of the gold plated electrodes [1,3]. The purpose of this study is not to optimize the cell's performance but rather to visualize the water gradient across the membrane. We have an operational fuel cell, not an optimal fuel cell.

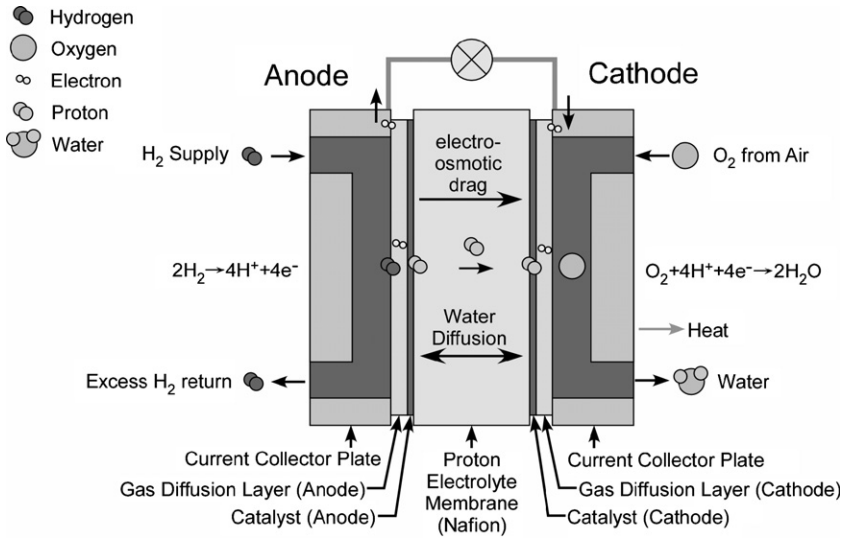

Fig. 1. A schematic of the polymer electrolyte membrane fuel cell (PEMFC). Chemical reactions occur at the anode and cathode. Two transport mechanisms, electro-osmotic drag and back-diffusion, control the water distribution.

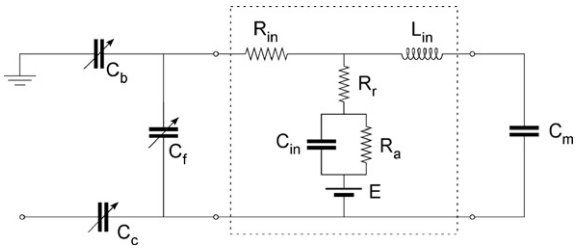

Fig. 2. The RF circuit diagram, with the operating fuel cell integrated into the circuit as the RF resonator. The equivalent circuit of the operating fuel cell consists of R_r, R_a, C_{in} and E. R_{in} and L_{in} represent the parallel plate transmission line. C_c, C_f, C_b and C_m, are capacitance values from conventional RF circuits to accomplish probe tuning and matching.

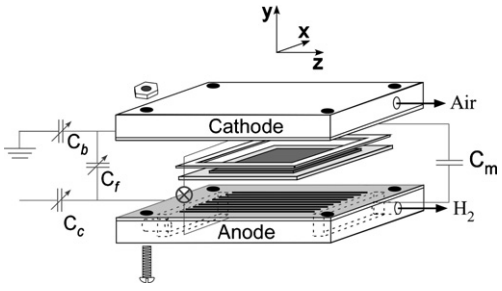

Fig. 3. Schematic of the homemade operating fuel cell with the outer load (⊗) and RF components connected. The Nafion layer is sandwiched between two catalyst sprayed gas diffusion layers to comprise a MEA. Two G10 fiberglass substrates, which support the PC boards, were machined, as shown by discrete lines in the figure, to generate paths for gas flow. Two homemade Teflon O-rings seal the cell. Only one, the frame shown above the Nafion, is illustrated. The entire apparatus was held together by 4 copper screws and tightened with a controlled torque.

3.3. B_1 field distribution

The influence of the slots in the plates on the B_1 field generated by the parallel plate resonator is revealed through in Fig. 5(b). It depicts the B_1 field distribution within the cross-section of a parallel plate resonator model, in which the top plate is cut with 10 slots, and the bottom plate is solid, Fig. 5(a). As illustrated, the current feeds in and out of the plates through points at the center of one edge, and yields a current flow parallel to the slots.

The simulated magnetic field, Fig. 5(b), in a cut-plane along x through the center of the resonator was calculated from the current distribution using the Biot–Savart law. The two white horizontal lines indicate the position of the plates within the cut-plane of Fig. 5(a). The B_1 field intensity, near the top plate, varies between the ridge and the gap, but the variation is less near the uncut bottom plate. The absence of current density yields a B_1 field beside the slots, which is approximately ten times less than that beside the intact plate. In addition, the B_1 fields inside the gas channels are very small, and will not efficiently excite the water or vapor in the channels.

The direction of the B_1 field produced by the parallel plate electrodes will be parallel to the GDLs. The finite penetration depth of the B_1 field into the GDL confines the excitation region to the interior of the fuel cell.

From the diagram of the cross-section of the cell, Fig. 5(c), the only free water which can be excited and detected would be water

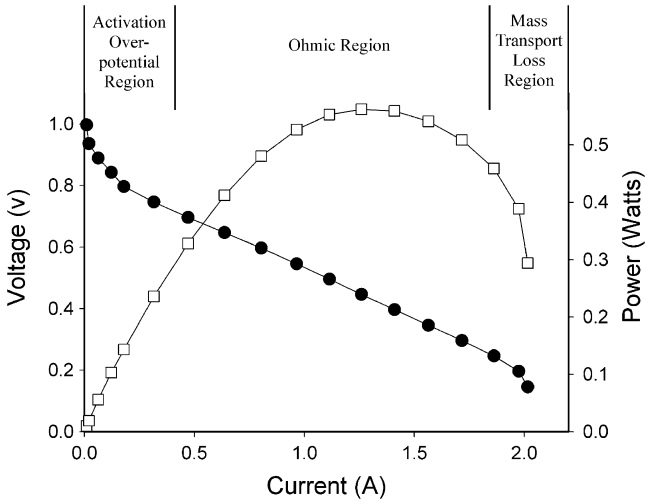

Fig. 4. The I–V polarization curve and the I–P curve of the homemade operating fuel cell were tested ex situ on a load station. The typical features of an operating fuel cell are observed, the activation overpotential region, the ohmic region and the mass transport loss region. The output power of the cell reaches its maximum when the current is 1.4 A.

trapped between the GDL and the Teflon O-ring. Although some free water must exist, it does not affect the image due to its relatively low levels.

3.4. Water content distribution across Nafion in an operational PEM fuel cell

In previous work [22], we observed that the MR relaxation times in Nafion vary with water content. The spatial gradient of water content across the Nafion will yield a spatial gradient of T_2, which must be resolved to generate quantitative water content maps.

The multiple echoes acquired yield spatially and temporally resolved T_2 and true water content maps [22]. Control experiments have revealed that the water T_2 decay in Nafion is always single exponential with realistic water content [22]. In this paper, single exponential fitting was always employed.

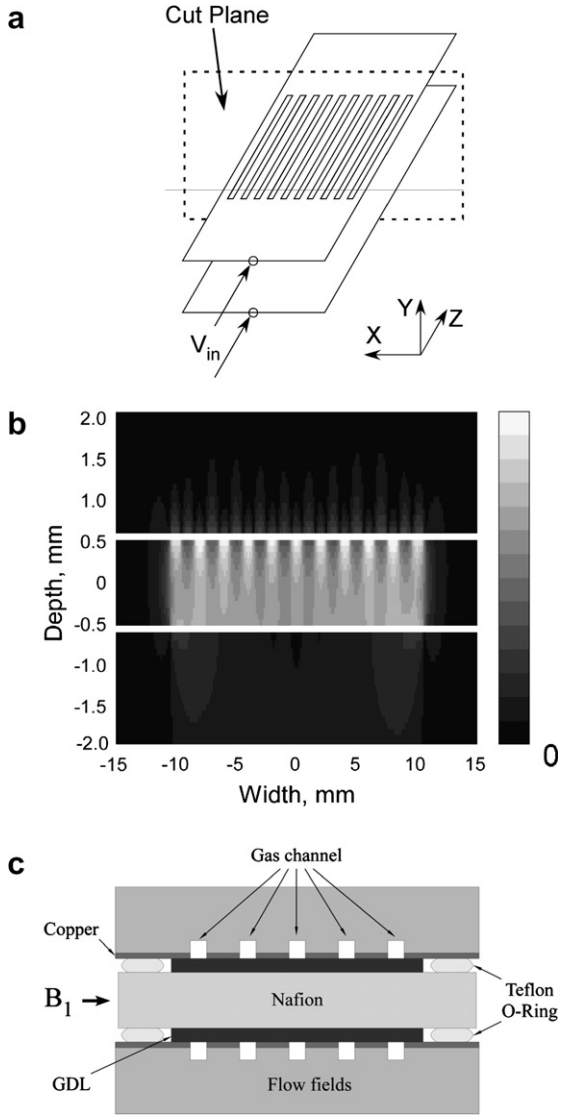

Fig. 5. (a) Simplified diagram of the parallel plate resonator for numerical simulation. (b) The calculated magnetic field from numerical simulation. Note the different horizontal and vertical position scales. The grey scale bar for magnetic field amplitude is in arbitrary units. Increasing the number of channels reduces the individual B_1 perturbation and yields a high quality lateral average for the depth measurements. (c) Schematic of the cross-section of the operating fuel cell. The electrode, with flow channels, behaves analogously to the slotted parallel plate depicted in (b). The B_1 field produced in (c) can be understood by reference to (b).

A series of one-dimensional water content profiles, were acquired to observe the fuel cell during the stages of activation, operation and dehydration. In each profile, the anode is located on the left with the cathode on the right. The reaction gases were fed in at a constant flow rate, 1.5 times the calculated stoichiometric quantity, with hydrogen gas at approximately 0.75 ml/s, and air at approximately 2 ml/s. Before flowing into the cell, both gases were bubbled through 60 °C water reservoirs. The experimental parameters were calibrated and the depth encoding gradient was adjusted to be orthogonal to the sample plane [19], before admitting the gases. A 3 Ω carbon resistor, directly connected to the electrodes, was employed as the outer load. The resistor was set inside the magnet to improve the SNR by shielding the assembly from external RF noise in these experiments. No experimental I–V polarization curve was therefore obtained in situ. At the commencement of the experiment, when the reactant gas flow began, the Nafion was relatively dry, with a small amount of water homogeneously distributed across the membrane, as illustrated in Fig. 6.

3.4.1. Stage 1: fuel cell activation

The relatively dry Nafion was hydrated by the reactant gas flow. Due to finite water in the Nafion, a low order operation of the fuel cell was anticipated.

At this stage, the anode signal in the profiles generated by the second echoes is too small to permit T_2 fitting. Only the first echo profiles are displayed in Fig. 6 to illustrate the distribution of the water signal. The signal close to the anode side at 0.1 h experimental time is lower than the initial water signal, which indicates water transport from the anode to the cathode across the membrane. This suggests electro-osmotic drag, a typical feature of an operating fuel cell, is causing water migration to the cathode.

With time the water content close to the anode increased, from a relatively dry state, while the water content close to the cathode remained at a high level from the very beginning of the measurement. A high early water content at the cathode is anticipated because of water production at the cathode. The MRI signal profile becomes increasingly linear between the electrodes with time.

In general, the activation stage is distinguished from operation through the I–V polarization curve, which is unable to be obtained in this measurement. The evidence suggests low order operation of the fuel cell during activation.

3.4.2. Stage 2: fuel cell operation

Once the Nafion is fully saturated, there is a self-adjustment of the water content in the membrane, as the electro-chemical reaction proceeds.

According to the first echo profiles, Fig. 7(a), the signal on the anode side was stable, but the signal on the cathode side decreased with time. Eventually, the signal intensity is largely uniform between the anode and the cathode. As the first echo profiles are significantly T_2-weighted, the variable TE water content profiles were fit to determine the true water content distribution. $\rho_0(y)$ at the edges of the profile cannot be determined due to difficulty fitting the data. Fig. 7(b) presents the true water content, $\rho_0(y)$, variation. The initial water content decreases quite uniformly. The water content on the cathode side decreases the most; however, the true water content in the steady state, after 1 h of operation, is higher on the cathode side. This is in accord with common understanding of the water distribution in an operating fuel cell. The cathode produces water during PEM fuel cell operation.

After approximately 1 h, the system reaches a quasi-steady state. As no apparent water redistribution is observed in the next 6 h, the next 60 first echo derived profiles at 1-h intervals, were averaged in groups of ten. The six resulting profiles, shown in Fig. 8(a), are stable in shape, and vary uniformly with time. An apparent signal intensity variation is observed after 5 h. After a

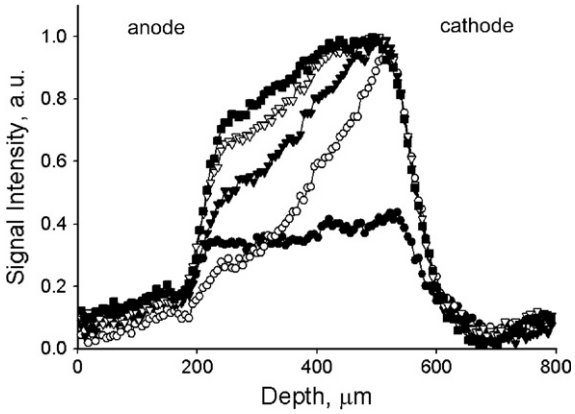

Fig. 6. Water signal across Nafion 1110 layer during fuel cell activation. Each profile was acquired in 6 min, and is spatially resolved by 128 pixels with 6 μm nominal resolution. The profiles were acquired during fuel cell activation. Experiments (●), (○), (▼), (▽), and (■) correspond to times of 0, 0.1, 0.2, 0.3 and 0.4 h after commencing gas flow. After an initial decrease close to the anode, the MR signal increases with time. The signal intensity close to the cathode is much higher than that close to the anode at early times.

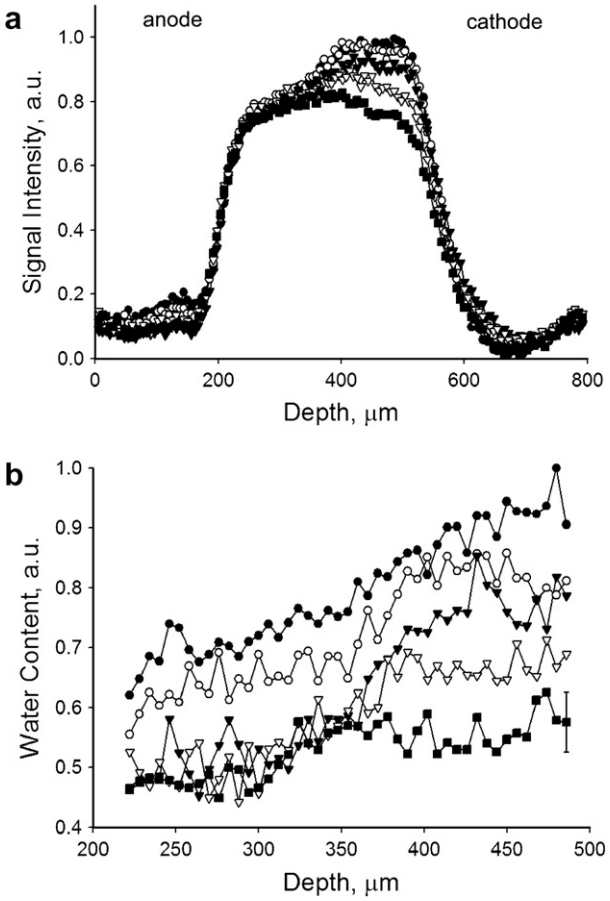

Fig. 7. (a) First echo images of the water content across the Nafion membrane during the first stage of fuel cell operation, which commenced at approximately 0.5 h after commencing gas flow. Five profiles spanning 0.7 h illustrate this process. Experiments (●), (○), (▼), (▽), and (■) correspond to experimental times of, 0.4, 0.5, 0.7, 0.9 and 1.1 h. With a stable signal close to the anode, the signal close to the cathode decreases with time. (b) True water content maps of (a) determined by relaxation time mapping. Experiments illustrated are the same as in (a). The true water content evolves with time but is generally higher near the cathode. Experimental fitting uncertainty is illustrated by the representative error bars at far right.

sudden decrease in the sixth hour, the signal in the seventh hour increases a little, and then in the eighth hour, the signal decreases again. The profile at 6 h overlaps with the profile of 8 h.

However, different water content variation is observed in Fig. 8(b), which contains six true water content profiles, averaged in the same manner as Fig. 8(a). The considerable difference between Fig. 8(a) and (b) indicates the signal variation observed in Fig. 8(a) is driven by T_2 change, and confirms the importance of T_2 mapping to extract true water content. In Fig. 8(b), the water content close to the anode side is stable, with a minimum around the 275–280 μm, the origin of which we do not understand. It is less than the water content on the cathode side. With time, the water content on the cathode side increases although the scatter is significant. As discussed previously, higher water content at the cathode is anticipated. No obvious water flooding effects at the cathode are observed.

The T_2 maps and true water content determination are both spatially and temporally resolved, with representative T_2 fitting shown in Fig. 9(a). Near ideal fitting confirms the assumption of single exponential decay. A composite T_2 profile, obtained by averaging all 60 T_2 maps, which cover 6 h of quasi-steady state operation, is shown in Fig. 9(b). The T_2 variation is quite small, in a range of 18.5–22 ms. Despite the limited dynamic range, a spatial variation is clear in Fig. 9(b), with the cathode side revealing slightly longer T_2.

A general observation from Fig. 9(b) is that regions of higher water content in the Nafion reveal longer T_2 values, which agrees with the study of MacMillan et al. [15,16]. The boundary conditions determined by the chemical reactions on the anode and cathode vary with operation. We emphasize that the sensitivity of T_2 to sample parameters, such as the local temperature, local electro-osmotic flow, and sample history, make a detailed interpretation of T_2 trends and absolute T_2 values problematic at present. Monitoring other fuel cell parameters, e.g. the I–V polarization curve, during the measurement to investigate the trends of water content and T_2 is required in further studies.

3.4.3. Stage 3: cathode dehydration

This stage of operation commenced after decreasing the RH of the incoming air to 12%, and decreasing the air temperature to 20 °C, with the flow rate maintained. The water content decreased in the membrane with dehydration by dry air flow. The first echo profiles, as shown in Fig. 10(a), were employed to illustrate the variation of the water content. The profile at 7 h was measured before the air inlet change. Immediately following this change the water content decreased throughout the Nafion. No reasonable water content profiles can be achieved, as we do not believe the scatter across the profiles is real. From the T_2 maps, Fig. 10(b), an obvious lifetime decrease is observed, from approximately 12 to 5 ms, which also indicates the membrane was dried.

4. Conclusion

The water content variation across a Nafion membrane in an operating fuel cell was monitored by high resolution MRI profiles. Three stages of the cell operation: activation, operation, and dehydration, were investigated. T_2 mapping reveals the true water content from the T_2 weighted profiles.

The high resolution data achieved in this experiment proves the parallel plate resonator is robust for high resolution depth imaging in PEM fuel cells, and its application to fuel cell MRI is very promising.

Measurements of this type may be used to validate existing numerical models of water transport in Nafion, and similar membranes, in operational PEM fuel cells. More experiments with

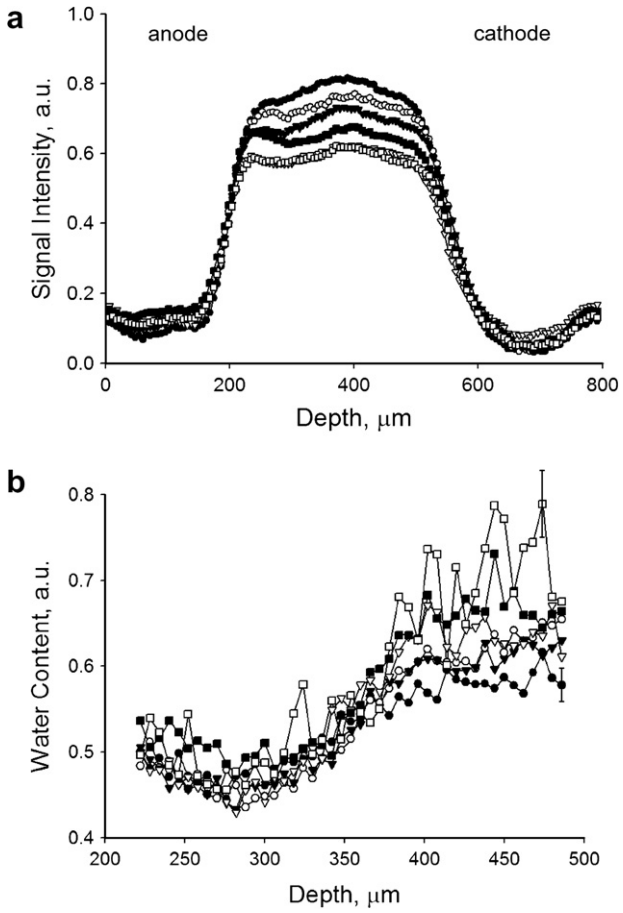

Fig. 8. (a) Water content profiles across the Nafion during quasi-steady state fuel cell operation, starting at approximately 1.2 h and lasting 6 h. Ten first echo MRI profiles were averaged over 1 h intervals to produce the profiles shown in (a). Profiles (●), (○), (▼), (▽), (■), and (□) correspond to time windows of, 1.1–2.1, 2.1–3.1, 3.1–4.1, 4.1–5.1, 5.1–6.1, 6.1–7.1 h. (b) True water content profiles determined by relaxation time mapping. The profiles displayed are also averaged. The profiles in (b) show stable water content close to the anode, with a higher water content near the cathode. Experimental uncertainties, due to fitting, are illustrated by the representative error bars at the far right.

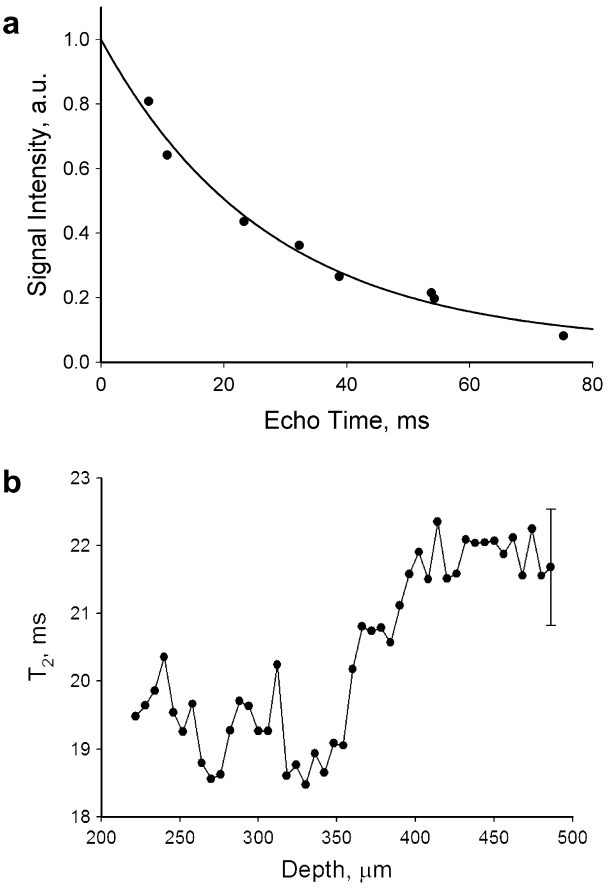

Fig. 9. (a) Representative T_2 fitting. The data of the pixel at 400 μm depth, at 1 h experimental time was selected. The single exponential decay is clear. The T_2 is approximately 27 ± 2 ms. (b) Composite T_2 map averaged over a 6-h time window. The T_2 values do not vary widely, but those close to the anode have a lower value than those close to the cathode. The standard error of the mean is illustrated by the representative error bar at the far right. No fitting uncertainty is presented.

a better designed fuel cell, and integrated load monitoring are required to perfect the measurements.

5. Experimental

5.1. Homemade operating fuel cell

Each plate of the homemade operating fuel cell, 5 cm in length and 4 cm in width, consists of a gold plated PC board and a substrate to which it is affixed. Thirty slots, 3 cm long, 0.5 mm width and 0.5 mm deep were cut, homogeneously distributed, in a 3 cm × 3 cm square area on the PC board for gas flow distribution, 1/16″ in thickness. The substrate, 3/8″ thick G10 fiberglass, was fabricated following the discrete line, shown in Fig. 3, to construct a path for flow. Each gas diffusion electrode (GDE), made by spraying the catalyst on a GDL, was cut into a 3.2 cm × 3.2 cm square, with the Nafion cut into a 3.5 cm × 3.5 cm square. The assembly was held by four copper bolts tightened to a constant torque.

5.2. Nafion and its preparation

The sample film, Nafion 1110, 250 μm thick, was purchased from Ion Power (New Castle, DE). The Nafion 1110 was cut to a desired size (1″ × 1″ for the depth imaging measurements), pretreated by heating in 3 ∼ 5 wt.% H_2O_2 solution at 80 °C for 1 h. The sample was then rinsed in deionized water at 80 °C for 1 h, and then, heated in 0.5 M H_2SO_4 at 80 °C for 1 h. The sample was finally cleaned by heating in deionized water at 80 °C for 1 h, to remove any possible chemical residues. The basic procedure was based on the work of Jalani [28] and Moore [29].

5.3. Cell evaluation

The cell voltages versus current densities curves were obtained with a Teledyne Medusa RD Fuel test station (Teledyne Energy Systems Inc., MD). The reactant gases, hydrogen and air, were externally humidified before entering the cell by bubbling through water at 60 °C. Constant reactant flow rates of 0.75 ml/s for hydrogen and 2 ml/s for air were employed.

5.4. MRI details

The multi-echo DHK SE SPI experiment was implemented on a Nalorac (Martinex, CA) 2.4 T 32 cm i.d. horizontal bore superconducting magnet. A water cooled 7.5 cm i.d. gradient set driven by Techron (Elkhart, IN) 8710 amplifiers, which provided 50 G/cm maximum gradients was employed for all experiments. Gradient G_y was chosen to be the principal phase encoding gradient. Misalignment of the spatial encoding gradient orthogonal to the sam-

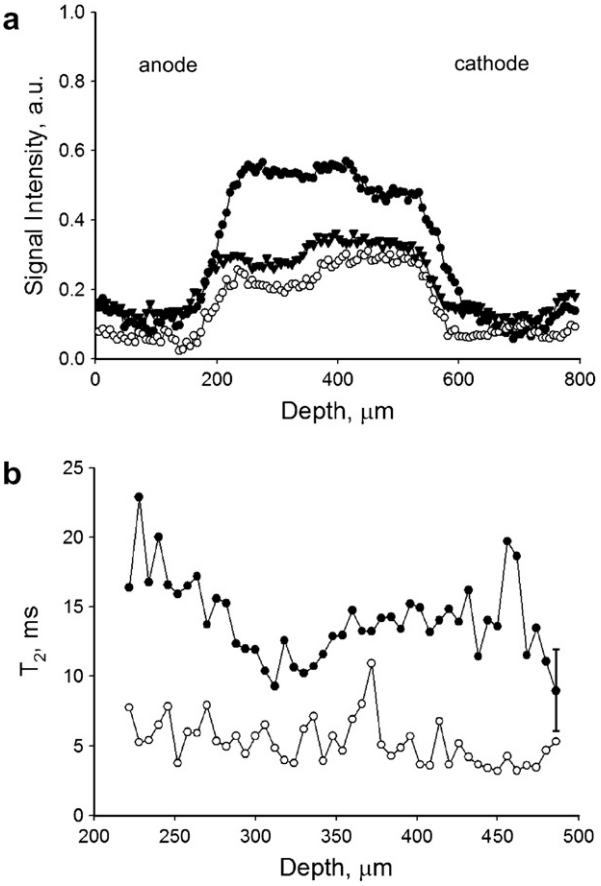

Fig. 10. (a) MRI first echo profiles illustrating fuel cell dehydration and cessation of operation. Experiments (●), (○) and (▼) correspond to experimental times of 7.1, 7.2, and 7.3 h. Experiment (●) is prior to adjustment of the air RH. A sudden signal drop occurred after the adjustment. (b) Corresponding T_2 maps. Experiments (●) and (○) correspond to experimental times of 7.1 and 7.2 h. The large decrease in T_2 indicates dehydration. The Nafion membrane was dried in 6 min. Experimental fitting uncertainty is illustrated by the representative error bars in the top profile at far right.

ple plane is the principal cause of resolution loss in these experiments. Gradients G_z and G_x were used as secondary phase encode gradients to orthogonalize the net depth encoding gradient to the sample plane. Gradient G_x also functioned as a spoiling gradient. The imaging console was a Tecmag (Houston, TX) Apollo for all experiments.

The RF probe, driven by a 2 kW AMT (Brea, CA) 3445 RF amplifier, was an operating fuel cell style resonator, shown in Fig. 2. The RF resonator was tuned to 100 MHz with three tuning capacitors, C_f, C_c and C_b in a standard series-parallel tank circuit. The fixed capacitor, C_m, illustrated in Fig. 2, was 1000 pF.

Due to the finite echo time required to achieve the desired resolution, 8 echoes were acquired with successive experiments of different TE, 7.75 and 10.75 ms respectively. Because the imperfect $90°_y$ and $180°_y$ pulses will induce incomplete signal compensation, only the odd echoes, yielding 8 echo profiles in total, were employed for T_2 mapping. Due to concern regarding probe detuning, the nominal 90° pulse width was monitored throughout the experiment, with the observation that it was well maintained at 39.5 μs. In all experiments, $180°_y$ pulses were executed as $90°_x 180°_y 90°_x$ composite pulses. The repetition time (TR) was maintained at 500 ms, which is $>5T_1$ for all echo trains, for all k-space points, in all experiments.

The nominal resolution for the measurements is the field of view divided by the number of pixels, approximately 6 μm, with a 800 μm FOV and 128 pixels. The encoding time, t_p, was 2.4 ms. Dwell times were set to 200 μs to narrow the filter width to 2500 Hz in all measurements. Sixteen echoes with different TE were obtained with an acquisition time of 360 s with a SNR of the first echo profile of approximately 40.

In high resolution depth imaging measurements, the Nafion film cannot be exactly positioned at the origin of the gradient G_y. Experimental profiles therefore wrap around the field of view (FOV) and are translated to the center of the FOV for display and subsequent data processing.

Acknowledgments

B.J.B. thanks NSERC of Canada for operating and equipment grants. B.J.B. also thanks the Canada Chairs program for a Research Chair in MRI of Materials (2002–2009). The MRI Centre is supported through an NSERC Major Facilities Access award. We thank R.P. MacGregor and Dr. Ben Newling for their assistance with the experiments, and NRC-IFCI for fabricating the operational fuel cell.

References

[1] W. Wielstich, H.A. Gasteiger, A. Lamm, Handbook of Fuel Cell—Fundamentals, Technology and Applications, John Wiley & Sons, New York, 2003.
[2] R.A. Lemons, Fuel cells for transportation, J. Power Sources 29 (1990) 251–264.
[3] G. Hoogers, Fuel Cell Technology Handbook, CRC Press, New York, 2000.
[4] T.E. Springer, T.A. Zawodzinski, S. Gottesfeld, Polymer electrolyte fuel cell model, J. Electrochem. Soc. 138 (1991) 2334–2342.
[5] T.A. Zawodzinski, C. Derouin, S. Radzinski, R.J. Sherman, V.T. Smith, T.E. Springer, Water uptake by and transport through Nafion® 117 membranes, J. Electrochem. Soc. 140 (1993) 1041–1047.
[6] Basic Research Needs for the Hydrogen Economy: Report on the Basic Energy Sciences Workshop on Hydrogen Production, Storage, and Use, Department of Energy, 2003.
[7] M. Eikerling, A.A. Kornyshev, Y. Kharkats, Y. Volfkovich, Phenomenological theory of electro-osmotic effect and water management in polymer electrolyte proton-conducting membranes, J. Electrochem. Soc. 145 (1998) 2684–2699.
[8] G.J. Janssen, A phenomenological model of water transport in a proton exchange membrane fuel cell, J. Electrochem. Soc. 148 (2001) 1313–1323.
[9] R.J. Bellows, M.Y. Lin, M. Arif, A.K. Thompson, D. Jacobson, Neutron imaging technique for in situ measurement of water transport gradients within Nafion in polymer electrolyte fuel cells, J. Electrochem. Soc. 146 (1999) 1099–1103.
[10] K. Teranishi, S. Tsushima, S. Hirai, Measurement of water distribution in polymer electrolyte fuel cell membrane by MRI, Therm. Sci. Eng. 10 (2002) 59–60.
[11] K. Teranishi, S. Tsushima, S. Hirai, Membrane thickness effect on PEFC's performance by measurement of water distribution, Therm. Sci. Eng. 11 (2003) 35–36.
[12] K.W. Feindel, L.P. LaRocque, D. Starke, S.H. Bergens, R.E. Wasylishen, In situ observations of water production and distribution in an operating H_2/O_2 PEM fuel cell assembly using ^{1}H NMR microscopy, J. Am. Chem. Soc. 126 (2004) 11436–11437.
[13] K.W. Feindel, S.H. Bergens, R.E. Wasylishen, The use of ^{1}H NMR microscopy to study proton-exchange membrane fuel cells, Chem. Phys. Chem. 7 (2006) 67–75.
[14] K.R. Minard, V.V. Viswanathan, P.D. Majors, L.Q. Wang, P.C. Rieke, Magnetic resonance imaging (MRI) of PEM dehydration and gas manifold flooding during continuous fuel cell operation, J. Power Sources 161 (2006) 856–863.
[15] B. MacMillan, A.R. Sharp, R.L. Armstrong, NMR relaxation in Nafion—the low temperature regime, Polymer 40 (1999) 2481–2484.
[16] B. MacMillan, A.R. Sharp, R.L. Armstrong, An NMR investigation of the dynamical characteristics of water absorbed in Nafion, Polymer 40 (1999) 2471–2480.
[17] T.A. Zawodzinski, M. Neeman, L.O. Sillerud, S. Gottesfeld, Determination of water diffusion coefficients in perfluorosulfonate ionomeric membranes, J. Phys. Chem. 95 (1991) 6040–6044.
[18] S.L. Codd, D.T. Howe, J.D. Seymour, E.H. Werre, S.C. Busse, E. Peterson, Magnetic resonance microscopy of heterogeneity in polymer electrolyte membranes, Appl. Magn. Res. 32 (2007) 13–24.
[19] A.V. Ouriadov, R.P. MacGregor, B.J. Balcom, Thin film MRI—high resolution depth imaging with a local surface coil and spin echo SPI, J. Magn. Reson. 169 (2004) 174–186.
[20] B.J. Balcom, R.P. MacGregor, S.D. Beyea, D.P. Green, R.L. Armstrong, T.W. Bremner, Single-point ramped imaging with T_1 enhancement (SPRITE), J. Magn. Reson. 123 (1996) 131–134.
[21] S. Gravina, D.G. Cory, Sensitivity and resolution of constant-time imaging, J. Magn. Reson. B 104 (1994) 53–61.

[22] Z. Zhang, Magnetic Resonance Imaging of Operational PM Fuel Cells and Related Materials, Ph. D. thesis, University of New Brunswick, 2008.
[23] P.J. McDonald, Stray field magnetic resonance imaging, Prog. NMR Spectrosc. 30 (1997) 69–101.
[24] M.D. Meadowcroft, S. Zhang, W. Liu, B.S. Park, J.R. Connor, C.M. Collins, M.B. Smith, Q.X. Yang, Direct magnetic resonance imaging of histological tissue samples at 3.0 T, Magn. Reson. Med. 57 (2007) 835–841.
[25] A. Weber, J. Newman, Transport in polymer-electrolyte membranes I. Physical models, J. Electrochem. Soc. 150 (7) (2003) A1008–A1015.
[26] A. Weber, J. Newman, Transport in polymer-electrolyte membranes II. Mathematical models, J. Electrochem. Soc. 151 (2) (2004) A316–A339.
[27] D.I. Hoult, The NMR receiver: a description, and analysis of design, Prog. NMR Spectr. 12 (1978) 41–77.
[28] N.H. Jalani, P. Choi, R. Datta, TEOM: a novel technique for investigating sorption in proton-exchange membranes, J. Mem. Sci. 254 (2005) 31–38.
[29] R.B. Moore, C. Martin, Chemical and morphological properties of solution cast perfluorosulfonate ionomers, Macromolecules 21 (1988) 1334–1339.